The Astrophysical Journal Letters, 976:L27 (12pp), 2024 December 1 https://doi.org/10.3847/2041-8213/ad7b17

Ionized Gas Kinematics with FRESCO: An Extended, Massive, Rapidly Rotating Galaxy at $z = 5.4$

Erica Nelson[1], Gabriel Brammer[2,3], Clara Giménez-Arteaga[2,3], Pascal A. Oesch[3,4], Rohan P. Naidu[5,34], Hannah Übler[6,7], Jasleen Matharu[2,3], Alice E. Shapley[8], Katherine E. Whitaker[3,9], Emily Wisnioski[10,11], Natascha M. Förster Schreiber[12], Renske Smit[13], Pieter van Dokkum[14], John Chisholm[15], Ryan Endsley[15], Abigail I. Hartley[1], Justus Gibson[1], Emma Giovinazzo[4], Garth Illingworth[16], Ivo Labbe[17], Michael V. Maseda[18], Jorryt Matthee[19,20], Alba Covelo Paz[4], Sedona H. Price[21], Naveen A. Reddy[22], Irene Shivaei[23], Andrea Weibel[4], Stijn Wuyts[24], Mengyuan Xiao[4], Stacey Alberts[25], William M. Baker[6,7], Andrew J. Bunker[26], Alex J. Cameron[26], Stephane Charlot[27], Daniel J. Eisenstein[28], Anna de Graaff[29], Zhiyuan Ji[25], Benjamin D. Johnson[28], Gareth C. Jones[26], Roberto Maiolino[6,7,30], Brant Robertson[31], Lester Sandles[6,7], Katherine A. Suess[31,32], Sandro Tacchella[6,7], Christina C. Williams[33], and Joris Witstok[6,7]

[1] Department for Astrophysical and Planetary Science, University of Colorado, Boulder, CO 80309, USA
[2] Niels Bohr Institute, University of Copenhagen, Jagtvej 128, DK-2200 Copenhagen N, Denmark
[3] Cosmic Dawn Center (DAWN), Niels Bohr Institute, University of Copenhagen, Jagtvej 128, København N, DK-2200, Denmark
[4] Department of Astronomy, University of Geneva, Chemin Pegasi 51, 1290 Versoix, Switzerland
[5] MIT Kavli Institute for Astrophysics and Space Research, 77 Massachusetts Avenue, Cambridge, MA 02139, USA
[6] Kavli Institute for Cosmology, University of Cambridge, Madingley Road, Cambridge, CB3 0HA, UK
[7] Cavendish Laboratory, University of Cambridge, 19 JJ Thomson Avenue, Cambridge, CB3 0HE, UK
[8] Department of Physics & Astronomy, University of California, Los Angeles, 430 Portola Plaza, Los Angeles, CA 90095, USA
[9] Department of Astronomy, University of Massachusetts, Amherst, MA 01003, USA
[10] Research School of Astronomy and Astrophysics, Australian National University, Canberra, ACT 2611, Australia
[11] ARC Centre of Excellence for All Sky Astrophysics in 3 Dimensions (ASTRO 3D), Australia
[12] Max-Planck-Institut für extraterrestrische Physik, Giessenbachstrasse 1, D-85748 Garching, Germany
[13] Astrophysics Research Institute, Liverpool John Moores University, 146 Brownlow Hill, Liverpool L3 5RF, UK
[14] Astronomy Department, Yale University, 52 Hillhouse Avenue, New Haven, CT 06511, USA
[15] Department of Astronomy, The University of Texas at Austin, 2515 Speedway, Stop C1400, Austin, TX 78712-1205, USA
[16] Department of Astronomy and Astrophysics, University of California, Santa Cruz, CA 95064, USA
[17] Centre for Astrophysics and Supercomputing, Swinburne University of Technology, Melbourne, VIC 3122, Australia
[18] Department of Astronomy, University of Wisconsin–Madison, 475 North Charter Street, Madison, WI 53706, USA
[19] Department of Physics, ETH Zürich, Wolfgang-Pauli-Strasse 27, Zürich, 8093, Switzerland
[20] Institute of Science and Technology Austria (IST Austria), Am Campus 1, Klosterneuburg, Austria
[21] Department of Physics and Astronomy and PITT PACC, University of Pittsburgh, Pittsburgh, PA 15260, USA
[22] Department of Physics and Astronomy, University of California, Riverside, 900 University Avenue, Riverside, CA 92521, USA
[23] Centro de Astrobiología (CAB), CSIC-INTA, Ctra. de Ajalvir km 4, Torrejón de Ardoz, E-28850, Madrid, Spain
[24] Department of Physics, University of Bath, Claverton Down, Bath, BA2 7AY, UK
[25] Steward Observatory, University of Arizona, 933 North Cherry Avenue, Tucson, AZ 85721, USA
[26] Department of Physics, University of Oxford, Denys Wilkinson Building, Keble Road, Oxford OX1 3RH, UK
[27] Sorbonne Université, CNRS, UMR 7095, Institut d'Astrophysique de Paris, 98 bis bd Arago, 75014 Paris, France
[28] Center for Astrophysics | Harvard & Smithsonian, 60 Garden Street, Cambridge, MA 02138, USA
[29] Max-Planck-Institut für Astronomie, Königstuhl 17, D-69117, Heidelberg, Germany
[30] Department of Physics and Astronomy, University College London, Gower Street, London WC1E 6BT, UK
[31] Department of Astronomy and Astrophysics, University of California, Santa Cruz, 1156 High Street, Santa Cruz, CA 95064, USA
[32] Kavli Institute for Particle Astrophysics and Cosmology and Department of Physics, Stanford University, Stanford, CA 94305, USA
[33] NSF's National Optical-Infrared Astronomy Research Laboratory, 950 North Cherry Avenue, Tucson, AZ 85719, USA
Received 2023 October 4; revised 2024 August 29; accepted 2024 September 12; published 2024 November 26

Abstract

With the remarkable sensitivity and resolution of JWST in the infrared, measuring rest-optical kinematics of galaxies at $z > 5$ has become possible for the first time. This study pilots a new method for measuring galaxy dynamics for highly multiplexed, unbiased samples by combining FRESCO NIRCam grism spectroscopy and JADES medium-band imaging. Here we present one of the first JWST kinematic measurements for a galaxy at $z > 5$. We find a significant velocity gradient, which, if interpreted as rotation, yields $V_{\rm rot} = 305 \pm 70\,{\rm km\,s^{-1}}$, and we hence refer to this galaxy as Twister-z5. With a rest-frame optical effective radius of $r_e = 2.25$ kpc, the high rotation velocity in this galaxy is not due to a compact size, as may be expected in the early Universe, but rather to a high total mass, $\log(M_{\rm dyn}/M_\odot) = 11.2 \pm 0.2$. This is a factor of roughly 10× higher than the stellar mass within r_e. We also observe that the radial Hα equivalent width profile and the specific star formation rate map from resolved stellar population modeling are centrally depressed by a factor of ∼1.5 from the center to r_e. Combined

[34] NASA Hubble Fellow.

with the morphology of the line-emitting gas in comparison to the continuum, this centrally suppressed star formation is consistent with a star-forming disk surrounding a bulge growing inside out. While large, rapidly rotating disks are common to $z \sim 2$, the existence of one after only 1 Gyr of cosmic time, shown for the first time in ionized gas, adds to the growing evidence that some galaxies matured earlier than expected in the history of the Universe.

Unified Astronomy Thesaurus concepts: High-redshift galaxies (734); Galaxy kinematics (602); Galaxy spectroscopy (2171); Galaxy bulges (578); Galaxy disks (589); Galaxy dynamics (591); Galaxy formation (595); Galaxy radii (617); Galaxy stellar content (621); Galaxy rotation curves (619); Galaxy evolution (594); Galaxy masses (607)

1. Introduction

Recently, with the James Webb Space Telescope (JWST), very massive galaxy candidates have been discovered in the first billion years of cosmic history (H. B. Akins et al. 2023; C. M. Casey et al. 2024; I. Labbé et al. 2023). This is surprising, as ΛCDM cosmology predicts that galaxies form hierarchically from the merging of smaller galactic units. If confirmed spectroscopically, the existence of very massive galaxies so early is hard to reconcile with current models. In some cases, the stellar mass of these galaxies pushes up against the total number of baryons available in the most massive halos (e.g., M. Boylan-Kolchin 2023). Further buttressing this idea is the prodigious number of bright galaxies with photometric redshifts $z > 10$ (or <500 Myr after the Big Bang), pointing again to a very early onset for formation (e.g., P. A. Oesch et al. 2016; M. Castellano et al. 2022; S. L. Finkelstein et al. 2022; R. P. Naidu et al. 2022; A. J. Bunker et al. 2023; C. A. Mason et al. 2023; S. Tacchella et al. 2023).

In addition to the surprising discovery at early times of massive and/or luminous galaxies is the discovery with JWST of apparently disk-dominated early galaxies (e.g., L. Ferreira et al. 2022; W. M. Baker et al. 2023; J. S. Kartaltepe et al. 2023; E. J. Nelson et al. 2023; B. E. Robertson et al. 2023). An abundance of disk-dominated galaxies at early cosmic time is unexpected in the context of studies based on projected axis ratios in <1.6 μm imaging with the Hubble Space Telescope (HST), which show that the fraction of galaxies with inferred disk-dominated morphologies drops dramatically at $z > 2$ (e.g., A. van der Wel et al. 2014; H. Zhang et al. 2019). It is also unexpected in the context of kinematic measurements showing that the majority of star-forming galaxies are less rotation-dominated at higher redshifts (e.g., N. M. Förster Schreiber et al. 2006, 2009, 2018; A. Gnerucci et al. 2011; E. Wisnioski et al. 2011, 2015, 2019; S. A. Kassin et al. 2012; S. H. Miller et al. 2012; L. J. Tacconi et al. 2013; R. C. Simons et al. 2017; O. J. Turner et al. 2017; H. L. Johnson et al. 2018; H. Übler et al. 2019; S. H. Price et al. 2020). These results are also surprising theoretically. First, in an expanding ΛCDM cosmology, the Universe is expected to be much denser at early times than at later times. With more galaxies per unit volume, the rate at which galaxies interact with one another should theoretically be much higher. In such a state of frequent bombardment, large disks would be unexpected. Second, owing to higher star formation efficiency or stellar feedback efficiency in high star formation surface density galaxies driving turbulence, early galaxies are expected to be more dispersion-supported (e.g., A. Pillepich et al. 2019; H. Übler et al. 2019; M. Girard et al. 2021). If more massive, more luminous, and larger disk galaxies really exist at early cosmic times, the Universe may be able to form mature galaxies earlier than we thought.

However, the implications of this early JWST work on our understanding of the early Universe remain hazy owing to observational uncertainties. First, very massive galaxies at very early times may be neither massive nor particularly early because both their redshifts and stellar population properties are uncertain. Their photometry could be affected by active galactic nuclei (AGN) or bursty star formation histories (e.g., R. Endsley et al. 2023; D. D. Kocevski et al. 2023; C. A. Mason et al. 2023; C. Papovich et al. 2023; L. Whitler et al. 2023). Second, the disky nature of these galaxies has also been inferred only from imaging. As this is just a 2D projection of a 3D object, there are degeneracies in the implied intrinsic shape. For instance, low axis ratios could reflect edge-on disks or prolate shapes (e.g., A. van der Wel et al. 2014).

Determining how common massive disk galaxies are at early times requires spectroscopy, which allows us to measure redshifts, masses, and kinematics. However, owing to the wavelength coverage of previous facilities, measurements of ionized gas kinematics using rest-frame optical emission lines like Hα and [O III] have thus far only been possible to $z < 3.5$ (e.g., N. M. Förster Schreiber et al. 2006; R. Genzel et al. 2008; G. Cresci et al. 2009; B. Epinat et al. 2009; D. R. Law et al. 2009; T. A. Jones et al. 2010; C. Mancini et al. 2011; E. Wisnioski et al. 2011, 2012, 2015; A. M. Swinbank et al. 2012; J. P. Stott et al. 2014; N. Leethochawalit et al. 2016; O. J. Turner et al. 2017; S. H. Price et al. 2020). Studies using millimeter and radio telescopes have begun to trace kinematics at $z > 3.5$ using, e.g., the [C II] 158 μm or CO line, which traces cooler gas, with some finding significant rotation (e.g., J. A. Hodge et al. 2012; R. Smit et al. 2018; K.-i. Tadaki et al. 2019; M. Neeleman et al. 2020; G. C. Jones et al. 2021; T. Tsukui & S. Iguchi 2021; E. Parlanti et al. 2023; A. Pope et al. 2023) and even surprisingly low velocity dispersions (e.g., F. Rizzo et al. 2020, 2021, 2023; F. Fraternali et al. 2021; F. Lelli et al. 2021; M. Y. Xiao et al. 2022).

With the launch of JWST, optical emission line kinematic measurements for galaxies at $z > 4$ have become possible for the first time. Here we present Hα kinematics of a massive, rapidly rotating galaxy at $z = 5.388$ using the NIRCam F444W grism. This galaxy is edge-on, extended, and fortuitously aligned with the grism dispersion direction and hence provides a simpler test of this methodology than the typically smaller, fainter, less well-aligned galaxies, which will require more sophisticated modeling (as in, e.g., A. de Graaff et al. 2024). In Section 2, we describe the observations and data reduction; in Section 3, we describe the methodology we use to measure kinematics and our kinematic results; and in Section 4, we give the spatial distribution of the line emission relative to the continuum. Finally, in Section 5, we discuss the implications of these results in the context of other recent work as well as the potential for using NIRCam grism spectroscopy to measure

kinematics with JWST. In this Letter, we assume the WMAP9 ΛCDM cosmology with $\Omega_M = 0.2865$, $\Omega_\Lambda = 0.7135$, and $H_0 = 69.32\,\mathrm{km\,s^{-1}\,Mpc^{-1}}$ (C. L. Bennett et al. 2013). All magnitudes in this Letter are expressed in the AB system (J. B. Oke 1974).

2. Data

The data in this Letter come from the FRESCO and JWST Advanced Deep Extragalactic Survey (JADES) programs in GOODS-S (D. J. Eisenstein et al. 2023; P. A. Oesch et al. 2023; M. J. Rieke et al. 2023). The object that forms the focus of our analysis, which we refer to as Twister-z5, has coordinates [R.A., decl.] = [53.10169662, −27.83616465] (J2000) and lies in the GOODS-S field. FRESCO is a 53.8 hr grism spectroscopic survey covering 124 arcmin^2 in the GOODS-N and GOODS-S fields (P. A. Oesch et al. 2023). It uses the NIRCam F444W grism, which has a maximal wavelength coverage of 3.8–4.9 μm and spectral resolution of $R \sim 1600$ to measure Hα [6563 Å] at the end of the epoch of reionization. The FRESCO GOODS-S data were taken between 2022 November 13 and 18, with an exposure time of 7 ks for the grism spectroscopy and 0.9 ks for the imaging at an orientation of ∼0° (V3PA in the range 353.9–0.6). Data reduction was conducted using the grizli software (G. Brammer 2023). A full description of the methods will be presented in G. Brammer et al. (2024, in preparation), but we summarize here for completeness. The rate files from MAST are aligned to a Gaia-matched reference frame; the direct images are then used to align their associated grism exposures. Bad pixels are masked, then individual exposures are combined.

We use a running median filter to subtract all continuum emission, leaving a frame with just emission lines. This method subtracts both the continuum from nearby sources that contaminates the spectrum as well as the continuum emission from the source of interest (D. Kashino et al. 2023; J. Matthee et al. 2023). This empirical method has the significant advantage of simplicity. However, it cannot be used if the continuum is of scientific interest, may oversubtract nearby emission lines (e.g., [N II]), and does not model underlying Balmer absorption. The continuum filtering is a two-step procedure. For the first pass, the continuum is subtracted from each row of the image using a running median filter with a 12 pixel central gap to avoid self-subtraction of emission lines. On the second pass, individual pixels with a signal-to-noise ratio (S/N) >3 are identified and masked; then the median filtering is run again. The position of the spectrum on the detector is computed based on the F444W image and spectral trace in the v4 grism configuration files.

In addition, imaging in eight filters (F090W, F115W, F150W, F200W, F277W, F356W, F410M, and F444W) was conducted as part of JADES (D. J. Eisenstein et al. 2023). Data are reduced as described in M. J. Rieke et al. (2023) and S. Tacchella et al. (2023). Specifically, the standard `jwst` pipeline was used with the CRDS context map `jwst_1039.pmap`. We used customized procedures to correct for "wisps" and 1/f noise, and a background subtraction has been performed on both the individual exposure level and the full mosaics. The mosaic images have been aligned to the Gaia-EDR3 catalog.

Photometry is performed on HST and JWST images point-spread function (PSF)–matched to the NIRCam F444W filter. Multiwavelength catalogs are generated using SExtractor (E. Bertin & S. Arnouts 1996). Sources are detected in dual-image mode using F444W as the detection image. Fluxes are measured in a 0.″16 aperture radius and corrected to total using the AUTO flux measurement and a small additional correction for the remaining flux outside this aperture based on the encircled energy for the PSF. All fluxes are corrected for Milky Way foreground extinction using E. L. Fitzpatrick & D. Massa (2007). Uncertainties on the fluxes are measured from the rms map and multiplied by a scale factor to account for noise not accounted for in the reduction pipeline. In order to determine this scale factor, we place circular apertures in empty regions of the image and compute the scatter among the flux measurements (see, e.g., K. E. Whitaker et al. 2011; R. E. Skelton et al. 2014).

Stellar population properties are derived using `prospector` (J. Leja et al. 2017, 2019; B. D. Johnson et al. 2021) with redshifts set to those inferred from the location of the Hα emission line in the grism spectrum of each galaxy. We adopt a 19 parameter physical model that includes redshift, stellar mass, stellar and gas-phase metallicities, star formation history, a two-component dust model (S. Charlot & S. M. Fall 2000), and emission from AGN (R. P. Naidu et al. 2022). We use FSPS (C. Conroy et al. 2009) with MIST stellar models (J. Choi et al. 2016). The fit is shown in Figure 1. Star formation rates (SFRs) are computed from the measured Hα fluxes assuming a G. Chabrier (2003) initial mass function with R. C. J. Kennicutt (1998). The fluxes are corrected for dust attenuation using empirical relations based on the UV slope (I. Shivaei et al. 2020). We note the caveat here that the conversion factor from Hα luminosity to SFR in R. C. J. Kennicutt (1998) is based on solar metallicity, and the vast majority of galaxies at these redshifts have subsolar metallicities, which can change this conversion factor by a factor of 2 (e.g., A. E. Shapley et al. 2023). Additionally, the empirical relations in I. Shivaei et al. (2020) were calibrated at $z \sim 2$ and may not be appropriate for $z \sim 5$.

One could question the use of the solar metallicity R. C. J. Kennicutt (1998) Hα conversion factor given that the vast majority of galaxies at this redshift appear to have significantly subsolar metallicities that can change the conversion factor by 2× (e.g., A. E. Shapley et al. 2023). Likewise, the I. Shivaei et al. (2020) relation was calibrated for $z \sim 2$ main-sequence galaxies, not those at $z \sim 5$ like these FRESCO sources.

Figure 2 shows the distribution of all galaxies with clearly detected Hα in the SFR–M_* plane. A locus of points is clearly detected, implying the existence of the star-forming main sequence at $z \sim 5$ as shown in A. E. Shapley et al. (2023). The galaxy that is the focus of the present study has $\log(M_*/M_\odot) = 10.4$ and $\mathrm{SFR} = 103 \pm 20\,M_\odot\,\mathrm{yr^{-1}}$, placing it at the high-mass end of this distribution and on the star-forming main sequence at this epoch.

We use the `GALFIT` software package (C. Y. Peng et al. 2002, 2010) to fit the size and shape of this galaxy accounting for the PSF following the procedure described in K. A. Suess et al. (2022) and E. J. Nelson et al. (2023). This fitting is performed on the direct images and the Hα map (see Section 3). An empirical PSF is constructed by stacking images of isolated point sources using EPSFBuilder in Photutils (see Z. Ji et al. 2024 for more details). We create a segmentation map to identify all sources to be modeled or masked. Galaxies that have centers within 3″ of the target

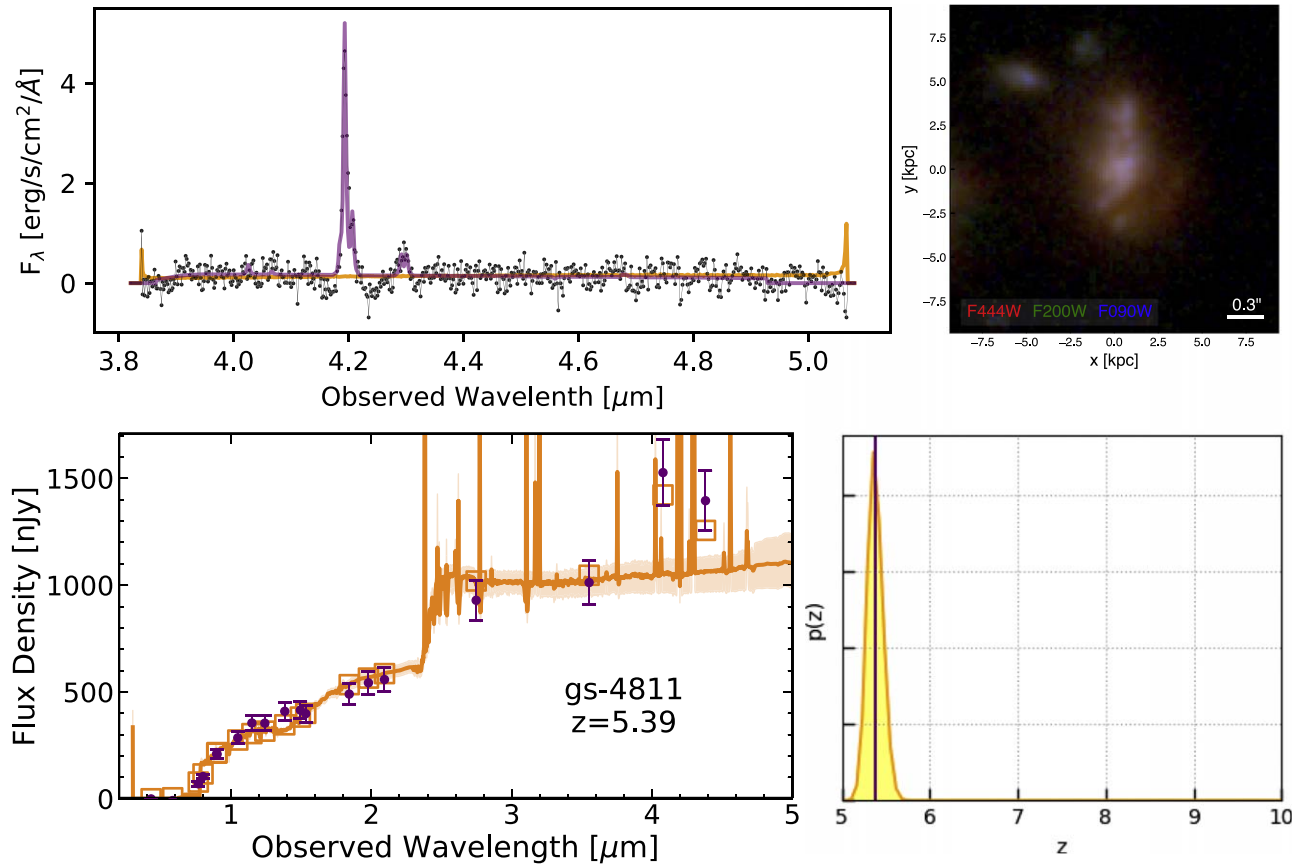

Figure 1. Top left: 1D spectrum of Twister-z5. Top right: three-color image F444W/F200W/F090W. Bottom left: photometry and best-fit stellar population synthesis model for Twister-z5. Bottom right: photometric redshift probability distribution function.

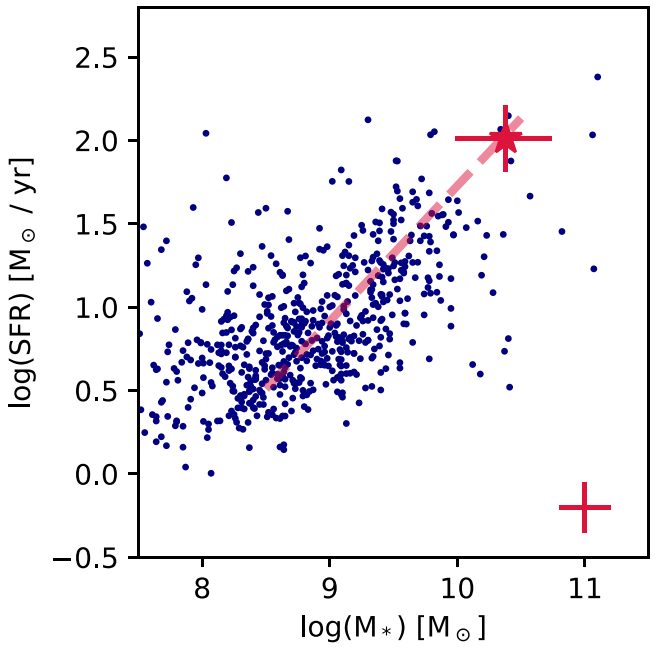

Figure 2. Star-forming main sequence for galaxies with grism spectroscopic redshifts $4.5 < z < 6$ in FRESCO with detected Hα. SFRs are computed from the measured Hα fluxes corrected for dust attenuation using empirical relations based on the UV slope (I. Shivaei et al. 2020). A fit to the SFMS from J. S. Speagle et al. (2014) is indicated by the red line for context. The typical measurement error is indicated by the plus sign in the lower right corner. Twister-z5, the galaxy featured in the present study, is at the very massive end of this distribution on the upper end of a continuation of the locus of points.

galaxy center and are less than 2.5 mag fainter are modeled simultaneously. Fainter and more distant galaxies are masked. With all sufficiently bright galaxies identified, we estimate and subtract the background in each stamp using the SExtractor background algorithm as implemented in `photutils`. For F444W, we find an effective radius $r_e = 2.2$ kpc, a Sérsic index $n = 1.75$, and an axis ratio $q = 0.5$. For the medium-band-derived Hα map, we find $r_e = 2.3$ kpc, $n = 0.2$, and $q = 0.25$.

3. Kinematics

A benefit or drawback of slitless grism spectroscopy, depending on the science goal, is that the dispersion axis contains not only spectral information, which is typical, but also spatial information. For HST/WFC3 or JWST/NIRISS, the spectral resolution of $R \sim 100$ corresponds to $\sim$1000 km s^{-1}. In the low-resolution regime, both axes of the emission line distribution are effectively spatial, and the continuum-subtracted line emission is essentially just an emission line flux map (e.g., P. G. van Dokkum et al. 2011; G. B. Brammer et al. 2012; E. J. Nelson et al. 2012, 2013, 2016; J. Matharu et al. 2021, 2022, 2023). The exception is broad-line AGN with line widths of >1000 km s^{-1}, which can be identified by their compact distribution in the spatial direction and extended distribution in the spectral direction (E. J. Nelson et al. 2012). However, the spectral resolution of the NIRCam F444W grism is much higher—$R \sim 1600$ at 4 μm—corresponding to a velocity dispersion of $\sigma \sim 80$ km s^{-1}. This resolution means that for galaxies with velocity gradients

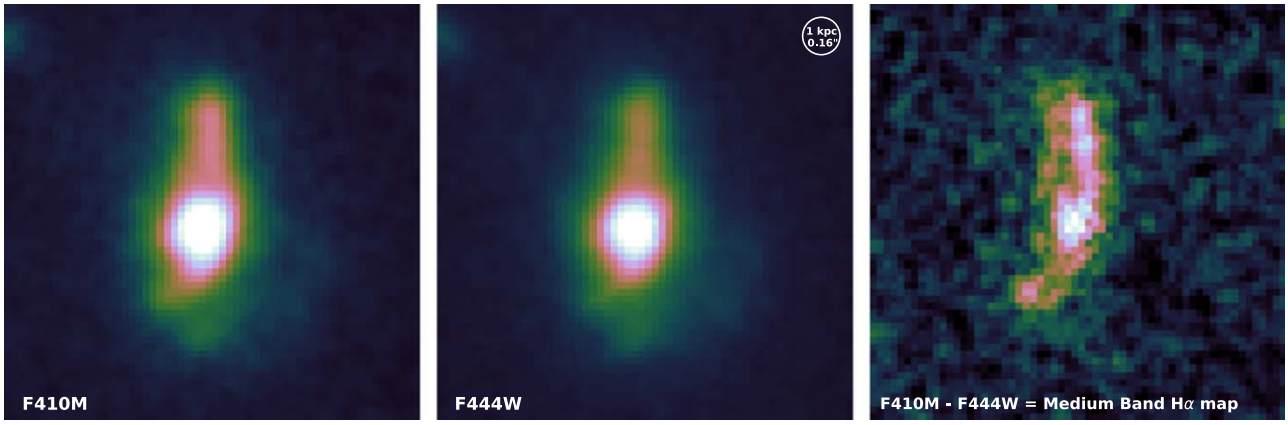

Figure 3. We infer the spatial distribution of Hα (right) from the difference between the F444W broadband filter (center) and F410M medium-band filter (left), which covers the Hα emission line at this redshift. The circle in the middle panel shows the size (FWHM) of the PSF.

of $>80\,\mathrm{km\,s^{-1}}$, we can place constraints on their kinematic properties in addition to the spatial distribution of their line emission.

Because the morphology of the emission line along the grism spectral axis is due to both the spatial and kinematic properties, additional data are needed to break the degeneracy. Here we use the F410M medium band, which covers the short-wavelength portion of the F444W filter in which the Hα line of this object falls. As shown in Figure 3, the difference between the F410M and F444W images essentially provides a map of the Hα line emission (e.g., C. C. Williams et al. 2023; S. Withers et al. 2023). To model the kinematics, we fit the light-weighted center of the Hα emission in each row of both the medium-band-derived map and the 2D grism spectrum. These data sets share a spatial centroid, so the measured difference in the light-weighted center is due to velocity. Hence, our velocity gradient is inferred by subtracting the medium-band Hα map light-weighted center from the grism image light-weighted center in each row. We define the systematic redshift such that the light-weighted center has zero velocity. This method is shown pictorially in Figure 4 alongside our results. The uncertainty on the velocity in each spatial pixel is calculated by bootstrap resampling the grism and medium-band images within the noise.

We measure an observed velocity difference $v_{\rm obs}$ from the maximum and minimum velocities by

$$v_{\rm obs} = \frac{1}{2}(v_{\rm max} - v_{\rm min}) = 295 \pm 60\,\mathrm{km\,s^{-1}}$$

as in, e.g., E. Wisnioski et al. (2015). We note that these minimum and maximum velocity values are driven by data quality, not the physical properties of the galaxy. The velocity curve shows no evidence of a flattening or turnover, so these represent the maximum radii to which we have a sufficient S/N to robustly determine the center and width of the line emission (S/N $\gtrsim 5$). If this velocity gradient represents rotation (more on this below), the observed velocity difference must be corrected for inclination in order to reflect the intrinsic rotation velocity:

$$v_{\rm rot} = v_{\rm obs}/\sin i.$$

We use the axis ratio measured from the medium-band Hα image (see Section 2) to infer the inclination of the galaxy using

$$\cos^2 i = (q^2 - q_0^2)/(1 - q_0^2),$$

where $q = 0.25$ is the measured axis ratio and q_0 is the intrinsic axis ratio. As we do not in fact know the intrinsic axis ratio, we include the full range of possible intrinsic axis ratios in our error budget, a uniform distribution of q_0 with $0.05 < q_0 < q$. Because the measured axis ratio is 0.25, this correction is very small in practice regardless of the assumed q_0 (<5%). We find $v_{\rm rot} = 305 \pm 70\,\mathrm{km\,s^{-1}}$. If we instead use the axis ratio measured in F444W ($q_{\rm f444w} = 0.5$), the inclination correction is larger, yielding an inclination-corrected velocity of $v_{\rm rot} = 340 \pm 70\,\mathrm{km\,s^{-1}}$.

With the combination of a medium-band Hα map and grism spectrum, it is also possible to measure the line-of-sight velocity dispersion. The width of the line in the spectral direction is broadened by three things: the spectrograph line-spread function, the line-of-sight velocity dispersion of the Hα gas (including beam smearing), and the intrinsic spatial extent. The contribution of the line-spread function is well known, and the degeneracy between the velocity dispersion and spatial extent can be broken using the combination of the medium-band and grism data.

We fit a Gaussian to the emission line in each row of the Hα in both the medium-band map and grism image. These widths are shown in Figure 5. To infer the line-of-sight velocity dispersion, we subtract off the instrumental line-spread function and spatial width in quadrature. As shown in Figure 4, the galaxy has an average velocity dispersion of $\sim$100 $\mathrm{km\,s^{-1}}$ in the disk and $\sim$225 $\mathrm{km\,s^{-1}}$ in the center. The most obvious physical explanation for the higher central velocity dispersion is a dynamically hot bulge. Beam-smeared rotation could also play some role, but we note that the measured rotation curve is close to linear. The ratio of rotation to velocity dispersion in the disk, an oft-used metric for the dynamical state of a system, is $V/\sigma \sim 2$–3.

An observed velocity gradient can be an indication of either a rotating disk or a merger (see, e.g., E. Wisnioski et al. 2015; R. C. Simons et al. 2017). Kinematically, if the object is a disk, one expects a centrally peaked velocity dispersion, while in a merger, the velocity dispersion is expected to be higher on either side and dip in the center (see, e.g., E. Wisnioski et al. 2015). We see a centrally peaked velocity dispersion profile,

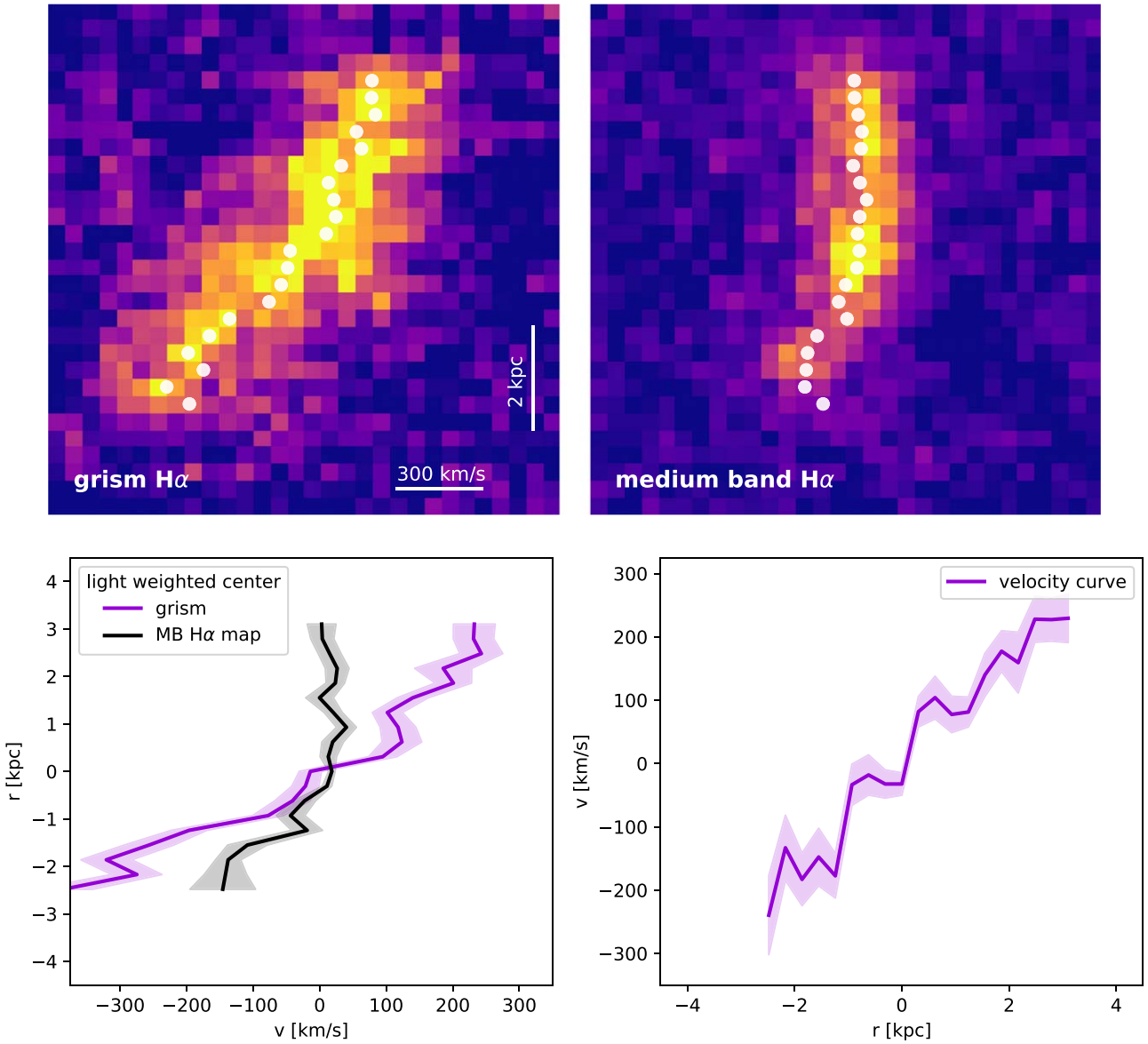

Figure 4. Velocity gradient. As described in Section 3, we fit the light-weighted center along the x-axis in the grism image, which corresponds to the dispersion direction (top left) and medium band Hα image (top right). The grism has a spectral resolution of $R \sim 1600$, meaning that the grism spectrum contains both spatial and spectral information across the dispersion direction. The difference between the grism and direct image centroids is the velocity in that spatial pixel. The error bars on the velocity curve are given by the difference between using the rest-UV emission and the F444W direct image.

which supports a disk rather than merger interpretation for our observed kinematics. Morphologically, asymmetry is often taken as an indication of a merger (e.g., J. M. Lotz et al. 2008). The broadband F444W imaging shows asymmetry around the brightness peak, and the Hα flux map shows an off-center brightness peak. While this could be interpreted as evidence for a merger, it is notable that many observations show that high-redshift star-forming galaxies have star-forming clumps that can be asymmetric (e.g., N. M. Förster Schreiber et al. 2006, 2009; E. Wisnioski et al. 2012). We interpret the observed velocity gradient as rotation but note the caveat that Twister-z5 may have experienced a merger, and whether it is virialized is uncertain.

We infer the dynamical mass of the system within the effective radius using our measured kinematics following S. H. Price et al. (2022). We compute the circular velocity $V_{\rm circ}$ accounting for turbulent pressure support with

$$V_{\rm circ} = (V_{\rm rot}^2 + \alpha\sigma_0^2)^{0.5}$$

(e.g., A. Burkert et al. 2010; E. Wuyts et al. 2016; N. M. Förster Schreiber et al. 2018; E. Wisnioski et al. 2018), where $\alpha = 3.36R/R_e$. The dynamical mass within the effective radius of this galaxy, if it can be described by a rotating disk, is

$$M_{\rm dyn} = k(R)\frac{V_{\rm circ}^2(R)R}{G}.$$

The virial constant $k(R)$ is dependent on the distribution of mass within the galaxy; we adopt $k(R = R_e) = 2.128$, which is the virial coefficient evaluated for $q = 0.4$ and $n = 1$, which invokes an elevated q to account for the spherical halo (as in, e.g., S. H. Miller et al. 2011; S. H. Price et al. 2020). We

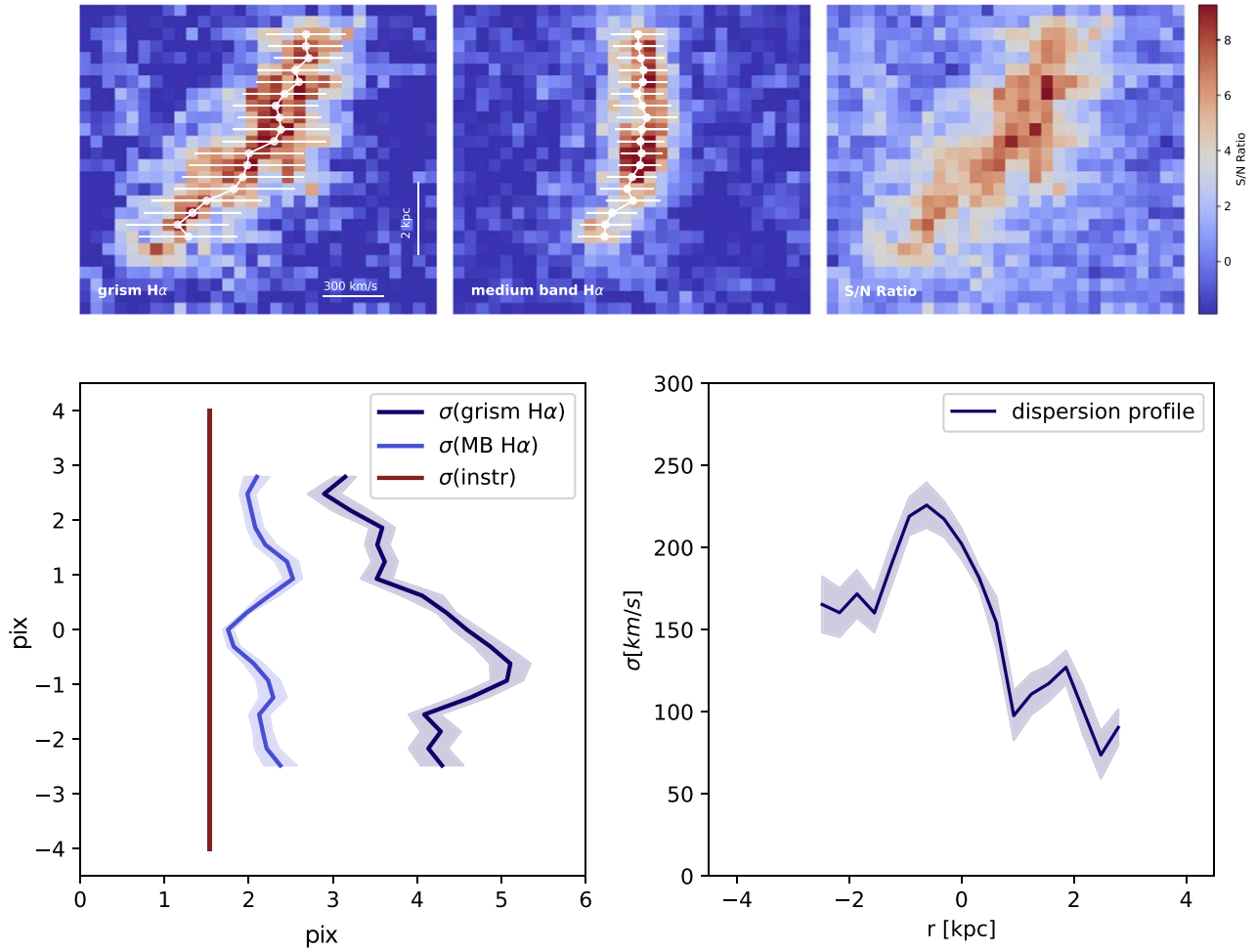

Figure 5. Velocity dispersion profile. As described in Section 3, the width of the Hα line in the spectral direction is broadened by three things: the line-of-sight velocity dispersion of the Hα gas (including beam smearing), the spectrograph line-spread function, and the intrinsic spatial extent. To measure the line-of-sight velocity dispersion, we subtract the latter two terms off in quadrature. Twister-z5 has a centrally peaked velocity dispersion cospatial with centrally concentrated light, perhaps indicative of a bulge. We measure a disk velocity dispersion of 50–150 km s^{-1}, which is likely an upper limit because dynamical forward-modeling has not been performed. The fact that the velocity dispersion peaks in the center and is lower in the disk suggests that the observed velocity gradient is likely due to rotation as opposed to a merger (for which one would expect peaks in the velocity dispersion on either side).

include the range of velocity dispersions measured in the disk in our dynamical mass uncertainty budget. We also remind the reader that we compute these quantities within the effective radius not because it represents the maximum rotation velocity but because beyond this radius we have insufficient signal to robustly measure kinematics.

We find a dynamical mass of $\log(M_{\rm dyn}) = 11.2 \pm 0.2$ within the effective radius. With a stellar mass of $\log(M_*) = 10.1 \pm 0.4$ within the effective radius, Twister-z5 has a much larger dynamical mass than stellar mass within the effective radius, although we note that the uncertainties are large. This stands to reason as the dynamical mass includes the dark matter and gas masses in addition to the stellar mass. We infer a gas mass of $\log(M_{\rm gas}) = 10.1 \pm 0.1$ by scaling the dust-corrected Hα SFR (as described in Section 2) with the Kennicutt–Schmidt relation using the effective radius of the Hα emission (R. C. J. Kennicutt 1998). Gas fractions are expected to rise dramatically to high redshift (L. J. Tacconi et al. 2020), so a gas fraction of $\sim$50% $\pm$ 20% is not surprising. Using these estimates of the mass components, we infer a baryonic mass that is $\sim 20^{+30}_{-10}$% of the total dynamical mass. At $1 < z < 3$, many studies of ionized gas or stellar kinematics find that massive galaxies ($\log(M_\star/M_\odot) \gtrsim 10$) are baryon-dominated within the galaxy scale, sometimes with inferred stellar masses alone that approach their inferred dynamical masses (e.g., N. M. Förster Schreiber et al. 2009, 2018; R. Bezanson et al. 2013; P. G. van Dokkum et al. 2015; L. Y. Alcorn et al. 2016; A. Burkert et al. 2016; J. P. Stott et al. 2016; E. Wuyts et al. 2016; G. Barro et al. 2017; R. Genzel et al. 2017; P. Lang et al. 2017; S. H. Price et al. 2020). On the other hand, the first study of the ionized gas kinematics of $z > 5$ galaxies with JWST finds dynamical masses an order of magnitude larger than stellar masses for low-mass galaxies ($\log(M_\star/M_\odot) \sim 7-9$; A. de Graaff et al. 2024). Larger samples of $z > 3$ galaxies covering a range of stellar masses and sizes will be needed to systematically study the baryon-to-dark-matter ratios of early disks.

4. The Spatial Distribution of Hα: Inside-out Growth

At $z \sim 5$–6, the F444W grism captures Hα emission, a tracer of star formation, and the F444W direct image captures the rest-frame *R*-band continuum, a reasonable proxy for stellar mass. As such, their quotient, the Hα equivalent width (EW (Hα)), can serve as a proxy for the specific SFR (SFR/M_*),

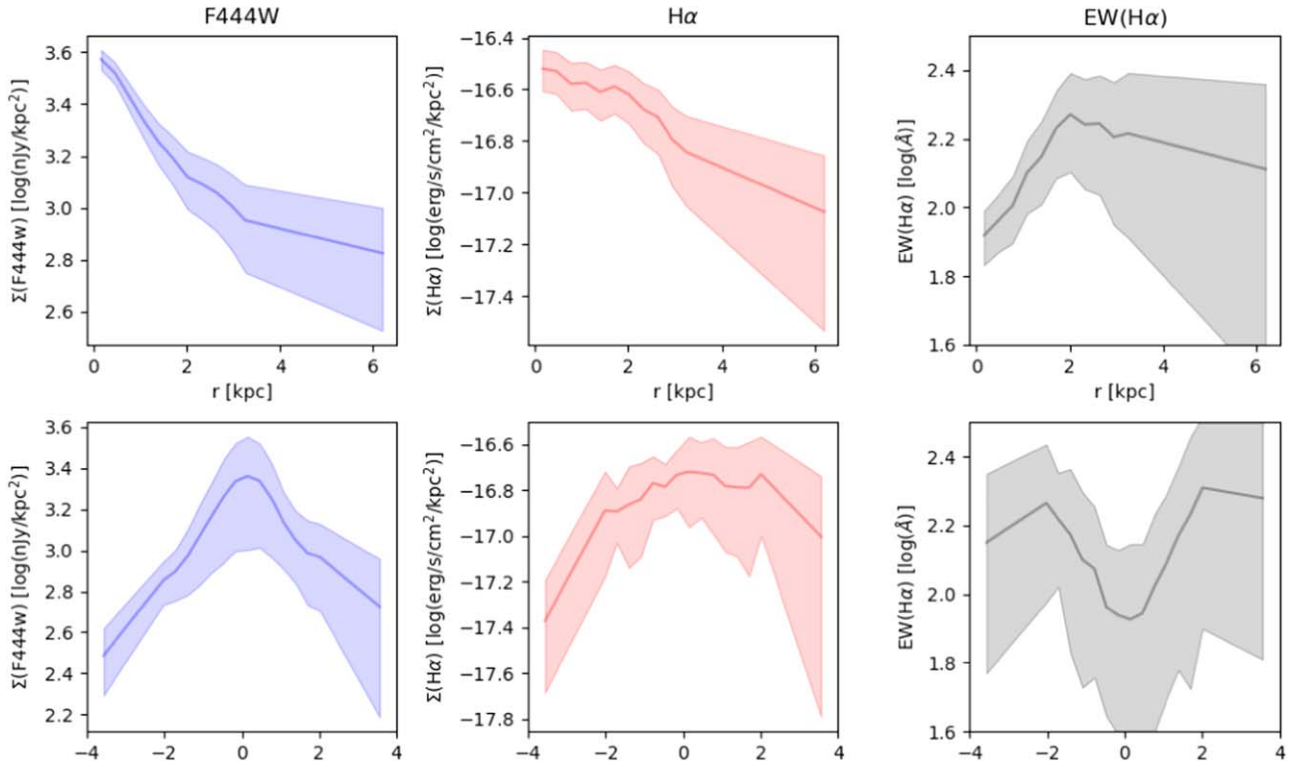

Figure 6. Surface brightness profiles of F444W (left), Hα (center), and the radial Hα equivalent-width profile (right) made as described in Section 4. The top row shows radially averaged profiles, while the bottom shows the full vertical profile. The Hα distribution is much less centrally concentrated than the 4.4 μm continuum emission resulting in an Hα equivalent-width profile that rises from the center to 2 kpc, consistent with this $z = 5.388$ galaxy growing inside out in a bulge–disk system.

which shows how the galaxy is growing (e.g., E. J. Nelson et al. 2013).

Owing to the impact of velocity on the observed morphology of Hα, we cannot measure a radial surface brightness profile in elliptical apertures. Instead, we effectively collapse the light distribution in both the direct and grism images along the detector axis corresponding to the dispersion axis in the grism image. In practice, to optimize the S/N of our profiles, we instead shift each row to the light-weighted centroid and sum along each row encompassing the effective semiminor axis. We subtract the Hα contribution from the F444W image. The resulting profiles are shown in Figure 6. The bottom row shows the profiles along the full vertical slice, and the top row shows them averaged in the upward and downward directions (similar to a radial profile).

The F444W light is much more centrally concentrated than the Hα emission; hence, the Hα equivalent-width profile rises sharply from the center to the effective radius at 2.25 kpc. Taking the EW(Hα) as a proxy for the specific SFR, the rising equivalent width we observe suggests that this galaxy is building mass more rapidly at $r \sim r_e$ than in the center. Further, the F444W profile is significantly steeper than the Hα profile. Because the Hα and continuum have the same wavelength, the attenuation they experience from diffuse dust is expected to be the same. While extra attenuation is expected toward H II regions (e.g., S. H. Price et al. 2014; N. A. Reddy et al. 2015), a variation in the quantity of extra attenuation toward H II regions would need to change as a function of radius to create the rising EW(Hα) observed. Given that this extra attenuation is surrounding birth clouds, this kind of geometric effect seems unlikely, but resolved measurements of Hβ would be needed to be sure (e.g., E. J. Nelson et al. 2016; B. Lorenz et al. 2023; A. E. Shapley et al. 2023). Further, even in the presence of significant dust attenuation, the Hα equivalent width is a reasonably good proxy for the specific SFR (e.g., E. J. Nelson et al. 2019). The most obvious interpretation of these features is that this galaxy is growing inside out with a star-forming disk surrounding a bulge with relatively suppressed star formation. The surprise, of course, is that this is not $z \sim 1$, where this structured inside-out growth is typical (e.g., E. J. Nelson et al. 2016), but $z > 5$.

We also perform spatially resolved spectral energy distribution (SED) fitting of the JWST imaging to determine if the conclusions hold with more sophisticated modeling following C. Giménez-Arteaga et al. (2023). Briefly, images in all JWST filters are PSF-matched to the F444W resolution, and the SED of each pixel is fit. Fits are performed with `BAGPIPES` (A. C. Carnall et al. 2018) with stellar population synthesis models by G. Bruzual & S. Charlot (2003), nebular emission with CLOUDY (G. J. Ferland et al. 2017), a P. Kroupa (2001) initial mass function, a D. Calzetti et al. (2000) attenuation curve, and a constant star formation history following A. C. Carnall et al. (2023) and C. Giménez-Arteaga et al. (2023). The redshift is fixed to the grism spectroscopic redshift. Visual extinction is allowed to vary, $A_V = 0$–3; the maximum age is 1 Myr–5 Gyr; and the metallicity is $Z = 0 - Z_\odot$, all with uniform priors. The resulting maps of stellar mass, SFR, and specific SFR are shown in Figure 7. As in the case of Hα equivalent width, the inferred specific SFR is lower in the center than at larger radii, suggesting that this galaxy is building from the inside out.

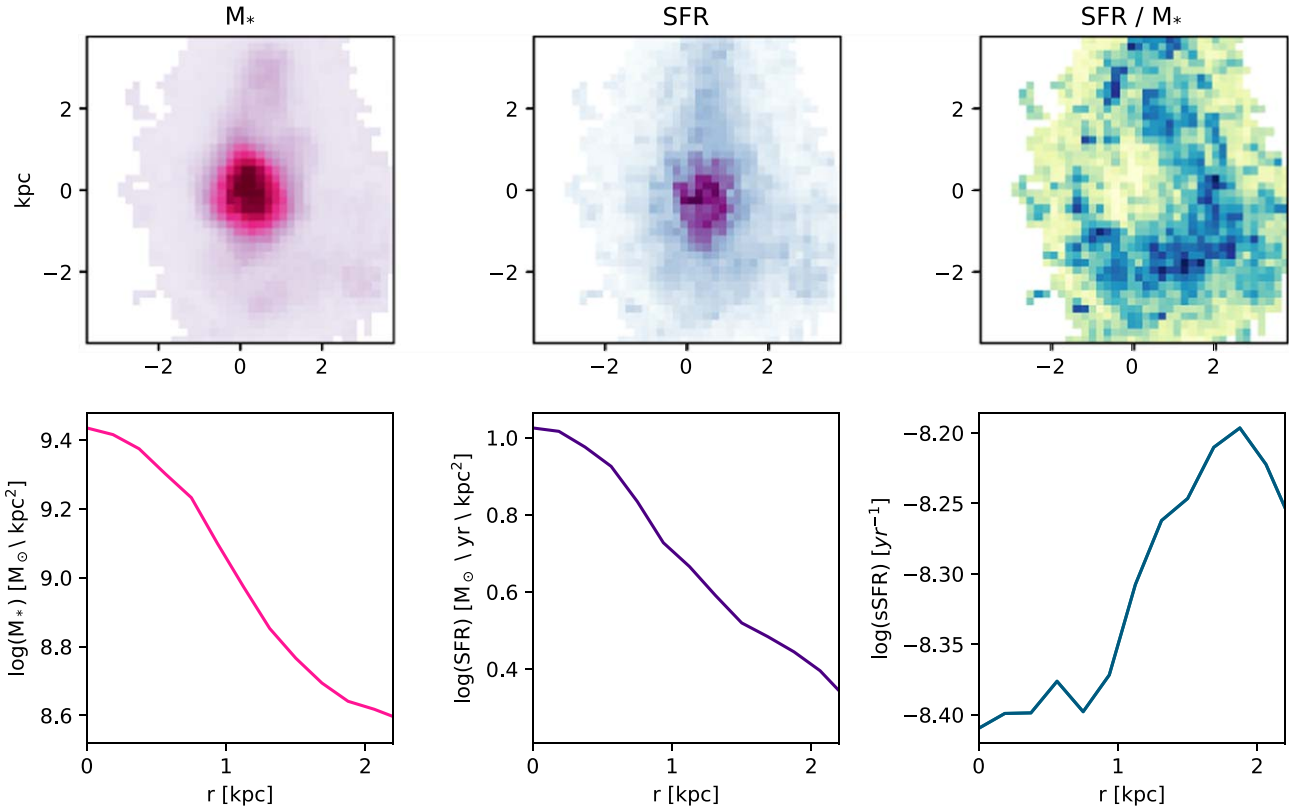

Figure 7. Resolved stellar populations based on SED fitting of the JWST imaging. The top row shows maps of the stellar mass (left), SFR (middle), and specific SFR (right) from spatially resolved SED modeling of the JWST images. The bottom row shows the radial surface density profiles of the stellar mass, SFR, and specific SFR, respectively. A clear central depression can be seen in the specific SFR, a feature that is typically seen in bulge–disk systems growing inside out.

5. Discussion

We measure kinematics and spatially resolved Hα emission for a $\log(M_*/M_\odot) = 10.4$ galaxy using FRESCO JWST/NIRCam spectroscopy combined with JADES medium-band imaging. We measure the effective radius of the rest-frame optical (0.55 μm) emission in the F356W filter, which is not expected to be dominated by line emission. This galaxy has a rest-optical effective radius of $r_e = 2.25$ kpc, comparable to the half-light radii of similar-mass galaxies at $z = 0.5$–1 (e.g., A. van der Wel et al. 2024), much larger than we anticipate for an early galaxy if galaxy sizes scale with the scale factor of the Universe. It is also significantly larger than one would expect based on existing measurements of the effective radius of galaxies as a function of redshift ($r_e(z)$), which finds $r_e \sim 1$ kpc at $z = 5.388$ (B. W. Holwerda et al. 2020). It has a rising EW(Hα) profile and a proxy for specific SFR and appears to be a bulge–disk system growing inside out. We measure a rotation velocity of 240 ± 50 km s^{-1}, similar to or greater than local massive spiral galaxies. In many ways, this appears to be a typical $z \sim 2$ disk galaxy. Oddly, it is not at $z \sim 2$ but $z = 5.388$. That massive, extended, rotating disk galaxies could exist at such early times is surprising, in particular because this does not appear to be a one-off situation but rather adds to the growing body of evidence for massive, extended, rotating disks seen in some studies of [C II] with the Atacama Large Millimeter/submillimeter Array (ALMA; e.g., J. A. Hodge et al. 2012; M. Neeleman et al. 2020; T. Tsukui & S. Iguchi 2021; E. Parlanti et al. 2023).

Considering the dynamical mass with respect to the stellar mass, Twister-z5 has a baryonic mass fraction of $\sim 20^{+30}_{-10}$% within the effective radius. With a dynamical mass of $\log(M_{\rm dyn}/M_\odot) = 11.2$, these mass fractions are somewhat smaller than galaxies with similar dynamical masses at $z = 1$–3 (e.g N. M. Förster Schreiber et al. 2018; S. H. Price et al. 2020). A number of studies find that galaxies become more baryon-dominated in their centers going from $z \sim 0$ to $z \sim 3$ (e.g., H. Übler et al. 2018; S. H. Price et al. 2020). However, at dynamical masses of $\sim 10^{11}$ $M_\odot$, the ratios of stellar-to-dynamical mass and baryonic-to-dynamical mass remain fairly constant (see, e.g., Figure 4 in S. H. Price et al. 2020). On the other hand, low-mass, high-redshift galaxies are possibly strongly dark-matter-dominated (A. de Graaff et al. 2024). More massive galaxies at $z \sim 7$ have been suggested to show a range in their baryonic-to-dynamical mass ratio depending on the luminosity-weighted age (M. W. Topping et al. 2022), although these measurements are based on spatially unresolved measurements of the [C II] emission line widths and therefore may be affected by mergers and nonvirial motions. One interpretation of this result is that the cosmic epoch may be more important than the total mass for determining how baryon-dominated the centers of galaxies are. This result is interesting in the context that some theoretical models find that galaxies transition from prolate to oblate when their centers become baryon-dominated (e.g., D. Ceverino et al. 2015). We emphasize here that the uncertainties on our mass measurements are large. Integral field spectsoscopy (IFU) would allow for a more robust interpretation.

We find $V/\sigma \sim 2$–3 for Twister-z5, meaning that although it is rotation-dominated, the velocity dispersion in the disk is much higher than that of local galaxies. This is likely to be an upper limit on the velocity dispersion, however, as we do not

forward-model the velocity field (as in, e.g., A. de Graaff et al. 2024), which can result in velocity dispersions that are biased high (e.g., F. Rizzo et al. 2022). That caveat noted, a mix of rotational and dispersion support is qualitatively consistent with many recent studies of Hα kinematics at the peak of the cosmic star formation history at $z = 1$–3 that have found higher high-velocity dispersions in the disks of higher-redshift galaxies (e.g., E. Wisnioski et al. 2015; A. M. Swinbank et al. 2017; O. J. Turner et al. 2017; H. Übler et al. 2019). A number of these studies find that V/σ declines with redshift to $\sim$1 at $z \sim 3$. Based on analytical modeling, H. Übler et al. (2019) suggest that the significant levels of turbulence in disks at $z > 1$ is driven by a combination of gravitational instabilities and stellar feedback (e.g., M. R. Krumholz et al. 2018; M. R. Varidel et al. 2020). Quantitatively, the rotation dominance we observe is higher than one would expect based on the extension of lower-redshift Hα studies. J. P. Stott et al. (2016) and O. J. Turner et al. (2017) find that the rotation-dominated fraction, which they define as $V/\sigma > 1$, declines with redshift as RDF $\propto z^{-0.2}$. If extrapolated, this relation implies that the rotation-dominated fraction for galaxies of similar mass at $z \sim 5.388$ is $\lesssim$10%. $V/\sigma \sim 2$–3 is, however, consistent with an extrapolation of the V/σ values predicted in the TNG50 cosmological hydrodynamical simulation (A. Pillepich et al. 2019). On the other hand, it is significantly lower than the values found by some studies of $z \sim 4$–5 galaxies in [C II] emission with ALMA, which find $V/\sigma \sim 10$ in some massive galaxies at this epoch (e.g., F. Rizzo et al. 2020, 2021; F. Fraternali et al. 2021; F. Lelli et al. 2021). With the objects having kinematic measurements in any tracer at $z > 5$ numbering less than 50, resolving this discrepancy will require kinematics for much larger samples in multiple tracers.

Although the kinematics of Twister-z5 appear typical for an extrapolation of cosmological simulations, the structure does not. The axis ratio distribution in the TNG50 simulation skews toward higher values than observed galaxies, suggesting that it has fewer prominent disks than the real Universe (J. S. Kartaltepe et al. 2023). Interestingly, there are almost no objects at $5 < z < 6$ in TNG50 with $n > 2$, suggesting that bulge–disk systems such as this are not expected in large numbers. Similar-mass galaxies in the TNG50 cosmological hydrodynamical simulation have a median observable effective radius of $\leqslant$1 kpc (L. Costantin et al. 2023), making an observed effective radius of $r_e = 2.25$ kpc much larger than expected. There are very few (if any) galaxies with $r_e > 2$, $n = 2$, and $b/a = 0.4$—i.e., a spatially extended bulge–disk system such as this. A number of studies find or predict that galaxies form bulges at early cosmic times and then build an extended stellar structure around it later (e.g., R. Bezanson et al. 2009; E. Nelson et al. 2014; P. G. van Dokkum et al. 2015; S. Wellons et al. 2015; A. Zolotov et al. 2015), which is qualitatively consistent with what we see in the the structure, kinematics, and particularly the specific SFR gradient of Twister-z5. However, a number of studies suggest that building an extended disk is hard at such early times. Disks at early cosmic epochs are expected to grow slowly, with formation times of $\sim$1.5 Gyr, due to instabilities that drive gas and stars to the center (e.g., D. Ceverino et al. 2015; M.-J. Park et al. 2019; L. Costantin et al. 2022).

This study and many others are pointing to the existence of mature galaxies at surprisingly early cosmic epochs. Remarkably luminous galaxy candidates have been found to $z \sim 13$ (e.g., P. A. Oesch et al. 2016; M. Castellano et al. 2022; S. L. Finkelstein et al. 2022; R. P. Naidu et al. 2022; A. J. Bunker et al. 2023; C. M. Casey et al. 2024; C. T. Donnan et al. 2023; Y. Harikane et al. 2023; S. Tacchella et al. 2023), and candidate massive galaxies with $M_* > 10^{10}\ M_\odot$ have been found at $z = 5$–9 (e.g., H. B. Akins et al. 2023; I. Labbé et al. 2023; M. Xiao et al. 2023). All of these unexpected sources require spectroscopic confirmation of their nature. Spectra obtained thus far reveal a mixed bag, with some redshifts holding (e.g., E. Curtis-Lake et al. 2023; G. Roberts-Borsani et al. 2023), some falling (e.g., P. Arrabal Haro et al. 2023), and some having remarkable mass or luminosity due to AGN instead of stars (e.g., D. D. Kocevski et al. 2023; R. Maiolino et al. 2024; J. Matthee et al. 2024; H. Übler et al. 2023). If a number of these results hold, the combination of JWST and ALMA might show us that mature galaxies form earlier than we previously thought possible. This study provides both redshift and dynamical confirmation of a massive galaxy at early cosmic time.

This Letter presents a new method for kinematic measurements with JWST, which has the potential to enable dramatic multiplexing for unbiased samples: slitless spectroscopy with medium-band imaging. With the fairly high spectral resolution of the NIRCam grism ($R \sim 1600$), this mode of spectroscopy could provide an efficient way to derive kinematic constraints on large samples of massive galaxies. Even stronger kinematic constraints could be placed using multiple grism dispersion directions. While validation tests need to be done against IFU data, this methodology could provide an exciting way to make kinematic measurements for large, unbiased samples of galaxies at early times, allowing us to understand their seemingly rapid early assembly.

Acknowledgments

We thank the reviewer and editorial staff for their excellent feedback and effort—the manuscript is much stronger as a result. Support for this work was provided by NASA through grant JWST-GO-01895 awarded by the Space Telescope Science Institute, which is operated by the Association of Universities for Research in Astronomy, Inc., under NASA contract NAS 5-26555. H.Ü. gratefully acknowledges support by the Isaac Newton Trust and by the Kavli Foundation through a Newton-Kavli Junior Fellowship. This work has received funding from the Swiss State Secretariat for Education, Research and Innovation (SERI) under contract No. MB22.00072, as well as from the Swiss National Science Foundation (SNSF) through project grant 200020_207349. The Cosmic Dawn Center (DAWN) is funded by the Danish National Research Foundation under grant No. 140. R.S. acknowledges an STFC Ernest Rutherford Fellowship (ST/S004831/1). R.P.N. acknowledges support for this work provided by NASA through the NASA Hubble Fellowship grant HST-HF2-51515.001-A awarded by the Space Telescope Science Institute, which is operated by the Association of Universities for Research in Astronomy, Inc., under NASA contract NAS5-26555. M.V.M. acknowledges support from the National Science Foundation via AAG grant 2205519 and the Wisconsin Alumni Research Foundation via grant MSN251397. R.M. also acknowledges funding from a research professorship from the Royal Society. A.J.B., A.J.C., and G.C.J. acknowledge funding from the "FirstGalaxies" Advanced Grant from the European Research Council (ERC) under the European Union's Horizon 2020 research and innovation

program (grant agreement No. 789056). I.L. acknowledges support by the Australian Research Council through Future Fellowship FT220100798. D.J.E. is supported as a Simons Investigator and by a JWST/NIRCam contract to the University of Arizona, NAS5-02015. R.M., J.W., L.S., and W.B. acknowledge support by the Science and Technology Facilities Council (STFC), the ERC through advanced grant 695671 "QUENCH," and the UKRI Frontier Research grant RISEandFALL. B.E.R. acknowledges support from the NIRCam Science Team contract to the University of Arizona, NAS5-02015. The research of C.C.W. is supported by NOIRLab, which is managed by the Association of Universities for Research in Astronomy (AURA) under a cooperative agreement with the National Science Foundation. The HST and JWST image mosaics of the FRESCO fields are released at MAST as a High Level Science Product (P. Oesch & D. Magee 2023).

Facilities: JWST, HST.

Software: Grizli, JWST calibration pipeline (H. Bushouse et al. 2023).

ORCID iDs

Erica Nelson https://orcid.org/0000-0002-7524-374X
Gabriel Brammer https://orcid.org/0000-0003-2680-005X
Clara Giménez-Arteaga https://orcid.org/0000-0001-9419-9505
Pascal A. Oesch https://orcid.org/0000-0001-5851-6649
Rohan P. Naidu https://orcid.org/0000-0003-3997-5705
Hannah Übler https://orcid.org/0000-0003-4891-0794
Jasleen Matharu https://orcid.org/0000-0002-7547-3385
Alice E. Shapley https://orcid.org/0000-0003-3509-4855
Katherine E. Whitaker https://orcid.org/0000-0001-7160-3632
Emily Wisnioski https://orcid.org/0000-0003-1657-7878
Natascha M. Förster Schreiber https://orcid.org/0000-0003-4264-3381
Renske Smit https://orcid.org/0000-0001-8034-7802
Pieter van Dokkum https://orcid.org/0000-0002-8282-9888
John Chisholm https://orcid.org/0000-0002-0302-2577
Ryan Endsley https://orcid.org/0000-0003-4564-2771
Abigail I. Hartley https://orcid.org/0000-0002-5891-1603
Justus Gibson https://orcid.org/0000-0003-1903-9813
Emma Giovinazzo https://orcid.org/0009-0004-3835-0089
Garth Illingworth https://orcid.org/0000-0002-8096-2837
Ivo Labbe https://orcid.org/0000-0002-2057-5376
Michael V. Maseda https://orcid.org/0000-0003-0695-4414
Jorryt Matthee https://orcid.org/0000-0003-2871-127X
Alba Covelo Paz https://orcid.org/0000-0002-9672-3005
Sedona H. Price https://orcid.org/0000-0002-0108-4176
Naveen A. Reddy https://orcid.org/0000-0001-9687-4973
Irene Shivaei https://orcid.org/0000-0003-4702-7561
Andrea Weibel https://orcid.org/0000-0001-8928-4465
Stijn Wuyts https://orcid.org/0000-0003-3735-1931
Mengyuan Xiao https://orcid.org/0000-0003-1207-5344
Stacey Alberts https://orcid.org/0000-0002-8909-8782
William M. Baker https://orcid.org/0000-0003-0215-1104
Andrew J. Bunker https://orcid.org/0000-0002-8651-9879
Alex J. Cameron https://orcid.org/0000-0002-0450-7306
Stephane Charlot https://orcid.org/0000-0003-3458-2275
Daniel J. Eisenstein https://orcid.org/0000-0002-2929-3121
Anna de Graaff https://orcid.org/0000-0002-2380-9801
Zhiyuan Ji https://orcid.org/0000-0001-7673-2257
Benjamin D. Johnson https://orcid.org/0000-0002-9280-7594
Gareth C. Jones https://orcid.org/0000-0002-0267-9024
Roberto Maiolino https://orcid.org/0000-0002-4985-3819
Brant Robertson https://orcid.org/0000-0002-4271-0364
Lester Sandles https://orcid.org/0000-0001-9276-7062
Katherine A. Suess https://orcid.org/0000-0002-1714-1905
Sandro Tacchella https://orcid.org/0000-0002-8224-4505
Christina C. Williams https://orcid.org/0000-0003-2919-7495
Joris Witstok https://orcid.org/0000-0002-7595-121X

References

Akins, H. B., Casey, C. M., Allen, N., et al. 2023, ApJ, 956, 61
Alcorn, L. Y., Tran, K.-V. H., Kacprzak, G. G., et al. 2016, ApJL, 825, L2
Arrabal Haro, P., Dickinson, M., Finkelstein, S. L., et al. 2023, Natur, 622, 707
Baker, W. M., Maiolino, R., Belfiore, F., et al. 2023, MNRAS, 518, 4767
Barro, G., Kriek, M., Pérez-González, P. G., et al. 2017, ApJL, 851, L40
Bennett, C. L., Larson, D., Weiland, J. L., et al. 2013, ApJS, 208, 20
Bertin, E., & Arnouts, S. 1996, A&AS, 117, 393
Bezanson, R., van Dokkum, P., van de Sande, J., Franx, M., & Kriek, M. 2013, ApJL, 764, L8
Bezanson, R., van Dokkum, P. G., Tal, T., et al. 2009, ApJ, 697, 1290
Boylan-Kolchin, M. 2023, NatAs, 7, 731
Brammer, G. 2023, grizli, v1.8.2, Zenodo, doi:10.5281/zenodo.7712834
Brammer, G. B., van Dokkum, P. G., Franx, M., et al. 2012, ApJS, 200, 13
Bruzual, G., & Charlot, S. 2003, MNRAS, 344, 1000
Bunker, A. J., Saxena, A., Cameron, A. J., et al. 2023, A&A, 677, A88
Burkert, A., Förster Schreiber, N. M., Genzel, R., et al. 2016, ApJ, 826, 214
Burkert, A., Genzel, R., Bouché, N., et al. 2010, ApJ, 725, 2324
Bushouse, H., Eisenhamer, J., Dencheva, N., et al. 2023, JWST Calibration Pipeline, v1.12.0, Zenodo, doi:10.5281/zenodo.8356444
Calzetti, D., Armus, L., Bohlin, R. C., et al. 2000, ApJ, 533, 682
Carnall, A. C., McLeod, D. J., McLure, R. J., et al. 2023, MNRAS, 520, 3974
Carnall, A. C., McLure, R. J., Dunlop, J. S., & Dave, R. 2018, MNRAS, 480, 4379
Casey, C. M., Akins, H. B., Shuntov, M., et al. 2024, ApJ, 965, 98
Castellano, M., Fontana, A., Treu, T., et al. 2022, ApJL, 938, L15
Ceverino, D., Dekel, A., Tweed, D., & Primack, J. 2015, MNRAS, 447, 3291
Chabrier, G. 2003, PASP, 115, 763
Charlot, S., & Fall, S. M. 2000, ApJ, 539, 718
Choi, J., Dotter, A., Conroy, C., et al. 2016, ApJ, 823, 102
Conroy, C., Gunn, J. E., & White, M. 2009, ApJ, 699, 486
Costantin, L., Pérez-González, P. G., Méndez-Abreu, J., et al. 2022, ApJ, 929, 121
Costantin, L., Pérez-González, P. G., Vega-Ferrero, J., et al. 2023, ApJ, 946, 71
Cresci, G., Hicks, E. K. S., Genzel, R., et al. 2009, ApJ, 697, 115
Curtis-Lake, E., Carniani, S., Cameron, A., et al. 2023, NatAs, 7, 622
de Graaff, A., Rix, H.-W., Carniani, S., et al. 2024, A&A, 684, A87
Donnan, C. T., McLeod, D. J., Dunlop, J. S., et al. 2023, MNRAS, 518, 6011
Eisenstein, D. J., Willott, C., Alberts, S., et al. 2023, arXiv:2306.02465
Endsley, R., Stark, D. P., Whitler, L., et al. 2023, MNRAS, 524, 2312
Epinat, B., Contini, T., Le Fèvre, O., et al. 2009, A&A, 504, 789
Ferland, G. J., Chatzikos, M., Guzmán, F., et al. 2017, RMxAA, 53, 385
Ferreira, L., Adams, N., Conselice, C. J., et al. 2022, ApJL, 938, L2
Finkelstein, S. L., Bagley, M. B., Haro, P. A., et al. 2022, ApJL, 940, L55
Fitzpatrick, E. L., & Massa, D. 2007, ApJ, 663, 320
Förster Schreiber, N. M., Genzel, R., Bouché, N., et al. 2009, ApJ, 706, 1364
Förster Schreiber, N. M., Genzel, R., Lehnert, M. D., et al. 2006, ApJ, 645, 1062
Förster Schreiber, N. M., Renzini, A., Mancini, C., et al. 2018, ApJS, 238, 21
Fraternali, F., Karim, A., Magnelli, B., et al. 2021, A&A, 647, A194
Genzel, R., Burkert, A., Bouché, N., et al. 2008, ApJ, 687, 59
Genzel, R., Förster Schreiber, N. M., Übler, H., et al. 2017, Natur, 543, 397
Giménez-Arteaga, C., Oesch, P. A., Brammer, G. B., et al. 2023, ApJ, 948, 126
Girard, M., Fisher, D. B., Bolatto, A. D., et al. 2021, ApJ, 909, 12
Gnerucci, A., Marconi, A., Cresci, G., et al. 2011, A&A, 528, A88
Harikane, Y., Ouchi, M., Oguri, M., et al. 2023, ApJS, 265, 5
Hodge, J. A., Carilli, C. L., Walter, F., et al. 2012, ApJ, 760, 11
Holwerda, B. W., Bridge, J. S., Steele, R. L., et al. 2020, AJ, 160, 154
Ji, Z., Williams, C. C., Tacchella, S., et al. 2024, ApJ, 974, 135
Johnson, B. D., Leja, J., Conroy, C., & Speagle, J. S. 2021, ApJS, 254, 22

Johnson, H. L., Harrison, C. M., Swinbank, A. M., et al. 2018, MNRAS, 474, 5076
Jones, G. C., Vergani, D., Romano, M., et al. 2021, MNRAS, 507, 3540
Jones, T. A., Swinbank, A. M., Ellis, R. S., Richard, J., & Stark, D. P. 2010, MNRAS, 404, 1247
Kartaltepe, J. S., Rose, C., Vanderhoof, B. N., et al. 2023, ApJL, 946, L15
Kashino, D., Lilly, S. J., Matthee, J., et al. 2023, ApJ, 950, 66
Kassin, S. A., Weiner, B. J., Faber, S. M., et al. 2012, ApJ, 758, 106
Kennicutt, R. C. J. 1998, ARA&A, 36, 189
Kocevski, D. D., Onoue, M., Inayoshi, K., et al. 2023, ApJL, 954, L4
Kroupa, P. 2001, MNRAS, 322, 231
Krumholz, M. R., Burkhart, B., Forbes, J. C., & Crocker, R. M. 2018, MNRAS, 477, 2716
Labbé, I., van Dokkum, P., Nelson, E., et al. 2023, Natur, 616, 266
Lang, P., Förster Schreiber, N. M., Genzel, R., et al. 2017, ApJ, 840, 92
Law, D. R., Steidel, C. C., Erb, D. K., et al. 2009, ApJ, 697, 2057
Leethochawalit, N., Jones, T. A., Ellis, R. S., et al. 2016, ApJ, 820, 84
Leja, J., Johnson, B. D., Conroy, C., van Dokkum, P. G., & Byler, N. 2017, ApJ, 837, 170
Leja, J., Johnson, B. D., Conroy, C., et al. 2019, ApJ, 877, 140
Lelli, F., Di Teodoro, E. M., Fraternali, F., et al. 2021, Sci, 371, 713
Lorenz, B., Kriek, M., Shapley, A. E., et al. 2023, ApJ, 951, 29
Lotz, J. M., Davis, M., Faber, S. M., et al. 2008, ApJ, 672, 177
Maiolino, R., Scholtz, J., Witstok, J., et al. 2024, Natur, 627, 59
Mancini, C., Förster Schreiber, N. M., Renzini, A., et al. 2011, ApJ, 743, 86
Mason, C. A., Trenti, M., & Treu, T. 2023, MNRAS, 521, 497
Matharu, J., Muzzin, A., Brammer, G. B., et al. 2021, ApJ, 923, 222
Matharu, J., Muzzin, A., Sarrouh, G. T. E., et al. 2023, ApJL, 949, L11
Matharu, J., Papovich, C., Simons, R. C., et al. 2022, ApJ, 937, 16
Matthee, J., Mackenzie, R., Simcoe, R. A., et al. 2023, ApJ, 950, 67
Matthee, J., Naidu, R. P., Brammer, G., et al. 2024, ApJ, 963, 129
Miller, S. H., Bundy, K., Sullivan, M., Ellis, R. S., & Treu, T. 2011, ApJ, 741, 115
Miller, S. H., Ellis, R. S., Sullivan, M., et al. 2012, ApJ, 753, 74
Naidu, R. P., Oesch, P. A., van Dokkum, P., et al. 2022, ApJL, 940, L14
Neeleman, M., Prochaska, J. X., Kanekar, N., & Rafelski, M. 2020, Natur, 581, 269
Nelson, E. J., Suess, K. A., Bezanson, R., et al. 2023, ApJL, 948, L18
Nelson, E. J., Tadaki, K.-i., Tacconi, L. J., et al. 2019, ApJ, 870, 130
Nelson, E., van Dokkum, P., Franx, M., et al. 2014, Natur, 513, 394
Nelson, E. J., van Dokkum, P. G., Brammer, G., et al. 2012, ApJL, 747, L28
Nelson, E. J., van Dokkum, P. G., Förster Schreiber, N. M., et al. 2016, ApJ, 828, 27
Nelson, E. J., van Dokkum, P. G., Momcheva, I., et al. 2013, ApJL, 763, L16
Oesch, P., & Magee, D. 2023, The JWST FRESCO Survey, STScI/MAST, doi:10.17909/GDYC-7G80
Oesch, P. A., Brammer, G., Naidu, R. P., et al. 2023, MNRAS, 525, 2864
Oesch, P. A., Brammer, G., van Dokkum, P. G., et al. 2016, ApJ, 819, 129
Oke, J. B. 1974, ApJS, 27, 21
Papovich, C., Cole, J., Yang, G. & Ceers Collaboration 2023, AAS Meeting Abstracts, 55, 102.02
Park, M.-J., Yi, S. K., Dubois, Y., et al. 2019, ApJ, 883, 25
Parlanti, E., Carniani, S., Pallottini, A., et al. 2023, A&A, 673, A153
Peng, C. Y., Ho, L. C., Impey, C. D., & Rix, H.-W. 2002, AJ, 124, 266
Peng, C. Y., Ho, L. C., Impey, C. D., & Rix, H.-W. 2010, AJ, 139, 2097
Pillepich, A., Nelson, D., Springel, V., et al. 2019, MNRAS, 490, 3196
Pope, A., McKinney, J., Kamieneski, P., et al. 2023, ApJL, 951, L46
Price, S. H., Kriek, M., Barro, G., et al. 2020, ApJ, 894, 91
Price, S. H., Kriek, M., Brammer, G. B., et al. 2014, ApJ, 788, 86
Price, S. H., Übler, H., Förster Schreiber, N. M., et al. 2022, A&A, 665, A159
Reddy, N. A., Kriek, M., Shapley, A. E., et al. 2015, ApJ, 806, 259
Rieke, M. J., Robertson, B. E., Tacchella, S., et al. 2023, ApJS, 269, 16
Rizzo, F., Kohandel, M., Pallottini, A., et al. 2022, A&A, 667, A5
Rizzo, F., Roman-Oliveira, F., Fraternali, F., et al. 2023, A&A, 679, A129
Rizzo, F., Vegetti, S., Fraternali, F., Stacey, H. R., & Powell, D. 2021, MNRAS, 507, 3952
Rizzo, F., Vegetti, S., Powell, D., et al. 2020, Natur, 584, 201
Roberts-Borsani, G., Treu, T., Mason, C., et al. 2023, ApJ, 948, 54
Robertson, B. E., Tacchella, S., Johnson, B. D., et al. 2023, ApJL, 942, L42
Shapley, A. E., Sanders, R. L., Reddy, N. A., Topping, M. W., & Brammer, G. B. 2023, ApJ, 954, 157
Shivaei, I., Reddy, N., Rieke, G., et al. 2020, ApJ, 899, 117
Simons, R. C., Kassin, S. A., Weiner, B. J., et al. 2017, ApJ, 843, 46
Skelton, R. E., Whitaker, K. E., Momcheva, I. G., et al. 2014, ApJS, 214, 24
Smit, R., Bouwens, R. J., Carniani, S., et al. 2018, Natur, 553, 178
Speagle, J. S., Steinhardt, C. L., Capak, P. L., & Silverman, J. D. 2014, ApJS, 214, 15
Stott, J. P., Sobral, D., Swinbank, A. M., et al. 2014, MNRAS, 443, 2695
Stott, J. P., Swinbank, A. M., Johnson, H. L., et al. 2016, MNRAS, 457, 1888
Suess, K. A., Bezanson, R., Nelson, E. J., et al. 2022, ApJL, 937, L33
Swinbank, A. M., Harrison, C. M., Trayford, J., et al. 2017, MNRAS, 467, 3140
Swinbank, A. M., Sobral, D., Smail, I., et al. 2012, MNRAS, 426, 935
Tacchella, S., Eisenstein, D. J., Hainline, K., et al. 2023, ApJ, 952, 74
Tacconi, L. J., Genzel, R., & Sternberg, A. 2020, ARA&A, 58, 157
Tacconi, L. J., Neri, R., Genzel, R., et al. 2013, ApJ, 768, 74
Tadaki, K.-i., Iono, D., Hatsukade, B., et al. 2019, ApJ, 876, 1
Topping, M. W., Stark, D. P., Endsley, R., et al. 2022, ApJ, 941, 153
Tsukui, T., & Iguchi, S. 2021, Sci, 372, 1201
Turner, O. J., Cirasuolo, M., Harrison, C. M., et al. 2017, MNRAS, 471, 1280
Übler, H., Genzel, R., Tacconi, L. J., et al. 2018, ApJL, 854, L24
Übler, H., Genzel, R., Wisnioski, E., et al. 2019, ApJ, 880, 48
Übler, H., Maiolino, R., Curtis-Lake, E., et al. 2023, A&A, 677, A145
van der Wel, A., Chang, Y.-Y., Bell, E. F., et al. 2014, ApJL, 792, L6
van der Wel, A., Martorano, M., Haussler, B., et al. 2024, ApJ, 960, 53
van Dokkum, P. G., Brammer, G., Fumagalli, M., et al. 2011, ApJL, 743, L15
van Dokkum, P. G., Nelson, E. J., Franx, M., et al. 2015, ApJ, 813, 23
Varidel, M. R., Croom, S. M., Lewis, G. F., et al. 2020, MNRAS, 495, 2265
Wellons, S., Torrey, P., Ma, C.-P., et al. 2015, MNRAS, 449, 361
Whitaker, K. E., Labbé, I., van Dokkum, P. G., et al. 2011, ApJ, 735, 86
Whitler, L., Endsley, R., Stark, D. P., et al. 2023, MNRAS, 519, 157
Williams, C. C., Tacchella, S., Maseda, M. V., et al. 2023, ApJS, 268, 64
Wisnioski, E., Förster Schreiber, N. M., Fossati, M., et al. 2019, ApJ, 886, 124
Wisnioski, E., Förster Schreiber, N. M., Wuyts, S., et al. 2015, ApJ, 799, 209
Wisnioski, E., Glazebrook, K., Blake, C., et al. 2011, MNRAS, 417, 2601
Wisnioski, E., Glazebrook, K., Blake, C., et al. 2012, MNRAS, 422, 3339
Wisnioski, E., Mendel, J. T., Förster Schreiber, N. M., et al. 2018, ApJ, 855, 97
Withers, S., Muzzin, A., Ravindranath, S., et al. 2023, ApJL, 958, L14
Wuyts, E., Wisnioski, E., Fossati, M., et al. 2016, ApJ, 827, 74
Xiao, M., Oesch, P., Elbaz, D., et al. 2023, arXiv:2309.02492
Xiao, M. Y., Wang, T., Elbaz, D., et al. 2022, A&A, 664, A63
Zhang, H., Primack, J. R., Faber, S. M., et al. 2019, MNRAS, 484, 5170
Zolotov, A., Dekel, A., Mandelker, N., et al. 2015, MNRAS, 450, 2327